Toward a Quantitative Relationship between Nanoscale Spatial Organization and Hybridization Kinetics of Surface Immobilized Hairpin DNA Probes

Qufei Gu[†], Huan H. Cao[‡], Yehan Zhang[‡], Haiyang Wang[†], Zachary J. Petrek[‡], Fukun Shi[|], Eric A. Josephs[§] and Tao Ye*[,‡]

[†]School of Engineering and [‡]Chemistry and Chemical Biology, School of Natural Sciences, University of California, Merced, Merced, California, 95343, United States
[|]Leibniz Institute for Plasma Science and Technology (INP), Greifswald, 17489, Germany
[§]Department of Nanoscience, University of North Carolina at Greensboro, Greensboro, North Carolina, 27401, United States

ABSTRACT: Hybridization of DNA probes immobilized on a solid support is a key process for DNA biosensors and microarrays. Although the surface environment is known to influence the kinetics of DNA hybridization, so far it has not been possible to quantitatively predict how hybridization kinetics is influenced by the complex interactions of the surface environment. Using spatial statistical analysis of probes and hybridized target molecules on a few electrochemical DNA (E-DNA) sensors, functioning through hybridization-induced conformational change of redox-tagged hairpin probes, we developed a phenomenological model that describes how the hybridization rates for single probe molecules are determined by the local environment. The predicted single-molecule rate constants, upon incorporation into numerical simulation, reproduced the overall kinetics of E-DNA sensor surfaces at different probe densities and different degree of probe clustering. Our study showed that the nanoscale spatial organization is a major factor behind the counter-intuitive trends in hybridization kinetics. It also highlights the importance of models that can account for heterogeneity in surface hybridization. The molecular level understanding of hybridization at surfaces and accurate prediction of hybridization kinetics may lead to new opportunities in development of more sensitive and reproducible DNA biosensors and microarrays.

KEYWORDS: *electrochemical DNA sensors, hybridization kinetics, single molecule measurement, spatial organization, atomic force microscope*
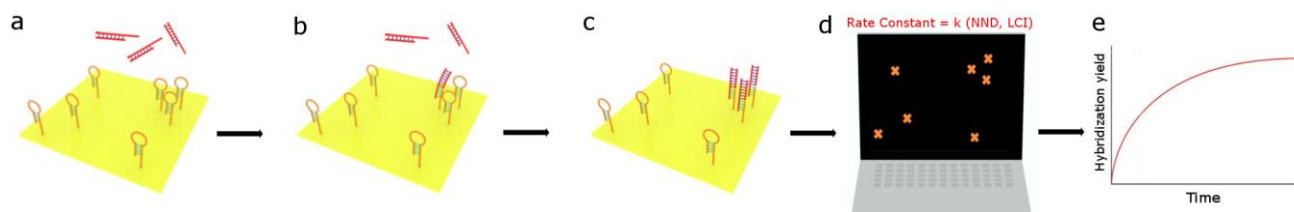
The sensitivity, selectivity, and reproducibility of biosensors and microarrays are often profoundly influenced by how surface-bound ligands and probes recognize target molecules.[1] As the surface environment is often crowded with ligand/probes as well as other molecules, such crowding interactions may alter the binding affinity and binding kinetics of interfacial molecular recognition in ways that are difficult to predict. A practical challenge in elucidating the effect of such interactions is that the spatial organization of these molecules, which determine these interactions, is often heterogeneous and exceedingly difficult to characterize at the spatial scale of 10 nm and below. Here we seek to understand how the nanoscale lateral distribution of hairpin DNA probes immobilized on a solid support influences surface hybridization, which is key to many DNA biosensors and microarrays that are being used for applications ranging from gene profiling,[1] *in vivo* monitoring,[2] to point of care diagnostics.[3-5] In addition, these surface-based DNA biosensors may also find utility in the rapid detection of pathogenic viruses, especially in the context of the COVID-19 pandemic.[6-8]

Many studies showed that as the average surface density of probe molecules increases,[9-16] crowding interactions such as steric hindrance and electrostatic repulsion not only reduce binding affinity, but also decelerate the binding kinetics. However, the average probe surface density is unlikely a reliable descriptor for crowding interactions when the lateral organization of probe molecules is often far from homogeneous.[17-19] Indeed, a handful of studies provided indirect evidence that heterogeneous probe densities may be the origin of significant device-to-device signal variabilities.[20-24]

Previously, we have enabled an atomic force microscopy (AFM) method to spatially resolve[25] the probe molecules and hybridized targets of electrochemical DNA (E-DNA) sensor surfaces, which utilize the conformational changes of surface-immobilized electroactive DNA probes upon target binding to detect analytes.[26] Single molecule imaging revealed an unexpected cooperative effect: the presence of neighboring hairpin probes may substantially accelerate target binding under specific circumstances, which contrasts with the common assumption that molecular crowding inhibits target capture.[11, 27-28] However, a direct, quantitative correlation between nanoscale lateral organization of the DNA probes and the overall hybridization kinetics has remained elusive. As the hybridization kinetics determines key figures of merit, such as limit of detection and detection speed, such a structure-function relationship is critically needed for rational engineering DNA-based sensors and microarrays.

Here we have combined high resolution imaging of the DNA probes and hybridized DNA target molecules with statistical models of single molecule rate constants to investigate how the overall kinetics of surface hybridization is influenced by the interfacial environment (Figure 1). We found that as the probe density increased from 1.83×10^{10} to 2.03×10^{11} probes/cm^2, the overall hybridization kinetics displayed a non-monotonic trend that is difficult to explain using the overall surface densities. However, the trend could be readily rationalized by examining the local probe

Figure 1. Schematic overview of the kinetics prediction approach. (a) The hairpin probes are immobilized on a single crystal Au surface and (b) hybridized with the targets. (c) The captured targets destabilize the neighboring hairpin probes and promote more hybridizations. (d) The spatial coordinates of the probes are extracted from analyzing the AFM images and then used to compute the single-probe rate constant using two key parameters in the nanoscale spatial patterns of probe molecules, nearest neighbor distance (NND), local crowding index (LCI). (e) The rate constants are implemented into numerical simulation to predict the hybridization kinetics.

spatial organization, such as nearest neighbor distance (NND), which is the nanoscale distance to the nearest DNA probe. Moreover, the overall kinetics of surface hybridization were largely reproduced by numerical simulations based on our statistical model of single molecule rate constants that included the effects of the nanoscale crowding at the surface. Simulation also successfully predicted divergent hybridization kinetics of two surfaces with similar overall surface densities, but different spatial patterns of probe molecules. Overall, our work provides direct evidence that the local probe spatial organization is a determining factor in the kinetics of surface hybridization of hairpin probes. By providing a new framework that connects the spatial patterns of DNA probes to the hybridization kinetics, our study represents a step toward elucidating the structure-function relationship of DNA biosensors and microarrays and rational engineering of devices that are capable of sensitive, rapid and highly reproducible detection of target molecules.
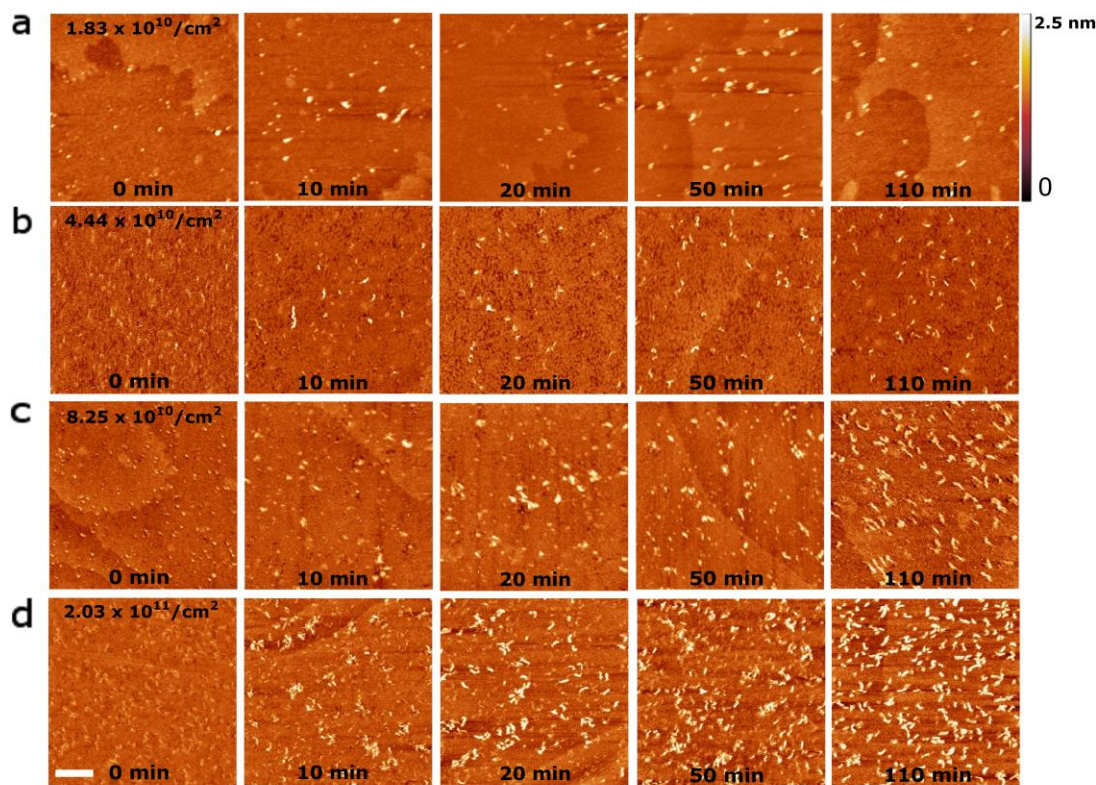
RESULTS AND DISSCUSSION

We chose to focus on E-DNA sensor surfaces[26] for a number of reasons. First, these sensor surfaces have been widely studied due to their high selectivity and potential in point of care diagnostics and *in vivo* monitoring.[2, 29] Second, these surfaces are an ideal model system for investigating how spatial organization of single molecules influences molecular recognition as highly ordered self-assembled monolayers may be used to minimize the impact of uncontrolled morphological and compositional heterogeneities.[18] Third, these surfaces are compatible with an imaging technique that can spatially resolve individual probes and captured DNA targets even when the inter-probe separation is less than 10 nm.[30] Stem-loop probes (a stem length of 6 bps and a loop length of 11 bases as shown in Table S1) modified with a thiol group at the 5' end and a methylene blue (MB) at the 3' end were immobilized onto a preassembled 11-mercaptoundecanoic acid (MUDA) self-assembled monolayer (SAM) on a single-crystal Au (111) support (Figure 1a). As shown previously,[26] the model surface with electroactive probes can produce electrochemical signals that are responsive to the target concentration. Details of the preparation and characterization of the interface can be found in the experimental method section.

A target molecule (T) consisting a 19-bp double-stranded tail, a 2-base spacer, and a 19-base single-stranded sticky-end (Table S1) was designed to facilitate AFM identification of the target-probe duplexes and mimic the footprint of many nucleic acid targets in clinical settings, which are often 150-300 nt in length.[1] Hybridization was performed by exposing the probe-modified single-crystal gold surface to the desired concentration of targets. To create a sufficiently representative data set for developing a

predictive model of single-molecule rate constants, we used AFM to measure the hybridization yields of the same biosensor surface at different time points and about 2000 individual probes were analyzed at each time point. Notably, because of the slow image acquisition rate of AFM, data were only collected at five time points for each surface density (Figure 2a-d). Future studies that utilize the improved throughput of fast-scanning AFM can address this limitation.[31] Figure 2a-d exhibited distinct conformations before (compact dot-like features) and after hybridization (extended worm-like features), allowing direct quantification of the hybridization yield by counting the number of hybridized probes and dividing it by the total number of probes, as illustrated by the symbols in Figure 3a. In all experiments, the targets were kept at a fixed concentration of 100 nM, to ensure a hybridization time scale of hours and minimize the aggregation of targets (Figure S1).[25] Kinetic traces, consisting of the hybridization yield as a function of time, were determined for probe coverages ranging from 1.83×10^{10} to 2.03×10^{11} probes/cm^2, or 183 to 2030 probes/μm^2. The hybridization likely proceeds via the formation of a partially hybridized probe-target complex.[32-33] However, as targets that are not tightly bound are washed away prior to AFM imaging, the AFM measures irreversibly captured targets. Nevertheless, the limitation is not assumed to have a significant impact on our ability to determine the influence of crowding on overall hybridization kinetics due to the following reasons. 1. Despite of the thorough rinsing after each hybridization step, the majority of the hybridized targets remained on the surface, which allows the use of Langmuir model assuming irreversible binding of target to the probe, as depicted in Figure 2a-d. 2. Our previous study showed an excellent correlation between the differential pulse voltammetry signal suppression (in situ measurement) and the hybridization yield measured by AFM.[25]

Figure 3a shows that the hybridization kinetics slowed down as the probe densities increased from 1.83×10^{10} to 8.25×10^{10} probes/cm^2, which appears to be consistent with the ensemble-averaging-based observations that increasing molecular crowding inhibits target binding.[9-15, 34] However, the hybridization kinetics accelerated when the probe density increased to 2.03×10^{11} probes/cm^2. The nonmonotonic trend is difficult to rationalize. If an increasing overall probe density reduces the accessibility of the probes to target molecules, surface hybridization should consistently decelerate as the probe density increases. If instead probe crowding destabilizes hairpin conformation and reduces the barrier for hybridization as shown in our previous study,[25] the hybridization kinetics should consistently accelerate as the probe density increases. Even if the trend results from the interplay between these two competing effects, *i.e.*, inhibition at low probe densities due to reduced accessibility, and acceleration at higher densities due to

2

Figure 2. Tracking time evolution of DNA surface hybridization. (a-d) Representative AFM images of the biosensor surface in the presence of 100 nM target DNA at 1.83×10^{10} (S1), 4.44×10^{10} (S2), 8.25×10^{10} (S3) and 2.03×10^{11} (S4) probes/cm². The scale bar is 100 nm.
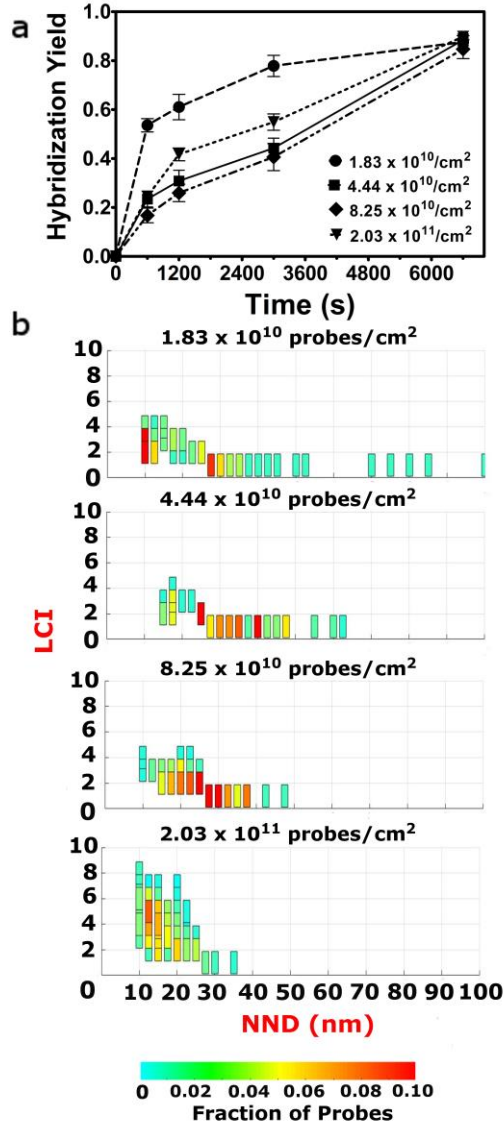
destabilization of the hairpins, it remains unclear why reduced accessibility is observed even at such low probe densities < 8.25×10^{10} probes/cm² (Figure 3a).

Since this counter-intuitive trend in binding kinetics is not readily explained by the overall probe density alone, we examined the impact of nanoscale spatial organization of probe molecules. Using single molecule imaging, our previous work found that individual probe molecules with low NNDs have faster hybridization kinetics, possibly because the hairpin destabilization by crowding interactions accelerates hybridization.[25] Moreover, even when the probes have similar NNDs, those with higher local crowding indices (LCIs), which describe crowding interactions beyond nearest neighbors by counting probe molecules within a radius 20 nm (equivalent to about twice the length of the probe), have faster hybridization rates.[25]

To investigate whether the local spatial organization of probe molecules can account for the observed counter-intuitive trends in overall kinetics at different overall probe densities, we categorized the probes according to their NNDs and LCIs and the fraction of each category is displayed in a color map (Figure 3b). Figure 3b presents an increase in the most probable NND (red and orange domains) from 10 nm to 40 nm while the corresponding LCIs remain 1 or 2, when the overall density increased from 1.83×10^{10} to 8.25×10^{10} probes/cm². This shift provides an alternative explanation for the slowdown of the overall kinetics with increasing overall density: the rising population of probes with high NNDs, which lead to lower rate constants. That a surface with a higher overall probe density has larger overall NNDs, i.e., less probe crowding, is rather unexpected. However, the probe immobilization process is not completely random. Although the insertion method, which insert DNA into a preformed SAM, is

known to produce a more uniform probe spatial pattern than the traditional backfilling method,[18] the AFM images in Figure S2 show that at the lowest surface density investigated (1.83×10^{10}/cm²), the immobilized probes preferentially cluster near the step edges of the underlying gold substrate (green arrows), where the SAM defects are concentrated. The formation of clusters is consistent with the observation that approximately 35% of probes possess a NND of 10 nm or less (Figure S3a), which is about twice the contour length of a hairpin probe (3-4 nm). Given that the surface tethered hairpin probes can rotate around their anchor points, this small portion of probes can experience repulsive interactions with the neighboring probes of which the anchor point is twice the contour length away. The NNDs are substantially smaller than those on a surface with complete spatial randomness, which was estimated by averaging over 100 simulations of random points patterns with the same sample size and area as the AFM data, as shown in Figure S3a. As the surface density of probe molecules further increases, such SAM defects are saturated, and an increasing number of DNA probes are inserted at random locations. Indeed, the NNDs of these surfaces are similar or higher than those of a surface with complete spatial randomness (Figure S3b-d). Therefore, the slower hybridization kinetics is caused by increased NNDs, which reduced crowding effect that may destabilize the hairpins. Moreover, as the overall density further increases to 2.03×10^{11} probes/cm², the most probable NND is reduced to 15 nm and the most probable LCI increases to 5. It should be noted that the majority of the probes possess NNDs smaller than that of 4.44×10^{10} and 8.25×10^{10} probes/cm², and thus the corresponding kinetic traces differ considerably from each other (Figure 3a). This acceleration in kinetics may also be ascribed to the abundance of probes with a high LCI of 5, whereas the surfaces with lower probe densities of 4.44×10^{10} and 8.25×10^{10} probes/cm² have LCI of 1 or 2.

3

Figure 3. Spatial statistical analysis of the biosensor surface. (a) Kinetics of the biosensor surface at 1.83×10^{10} (S1), 4.44×10^{10} (S2), 8.25×10^{10} (S3) and 2.03×10^{11} (S4) probes/cm². (b) Spatial organizations of the probes as a function of both NND and LCI at different probe densities. The color bar represents the range of fraction of probes.
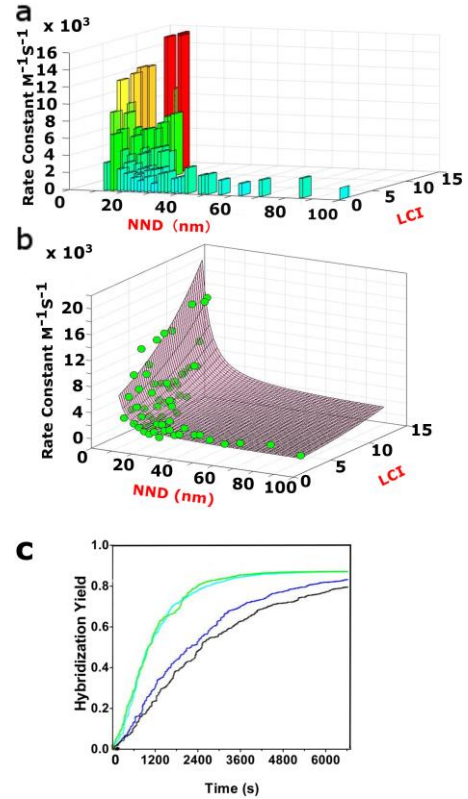
These spatial statistical analyses revealed that the local proximity-induced enhancement in target binding of the individual probes can qualitatively explain counter-intuitive trends in the overall hybridization kinetics of the E-DNA sensor surface. The next question is whether a quantitative relationship between the local probe spatial pattern and the overall kinetics can be established. To address this question, we built a phenomenological kinetic model to predict rate constants of probe molecules in different local environments as described by NNDs and LCIs (Figure 4). Then we incorporated the single-molecule rate constants predicted by our model into the numerical simulation (see SI for details), which allowed the prediction of the overall kinetics for a given probe spatial pattern and comparison with experimental data. As the surface hybridization is reaction-limited, as indicated by the small values of the Damköhler number (< 0.08 for all cases we considered, see details in SI), we extracted the rate constants from the first-order

Langmuir fitting of the kinetic curves in each of the categories of NNDs and LCIs mentioned above and displayed as a 2D histogram, as viewed in Figure 4a. The histogram demonstrates that the rate constant can vary by more than one order of magnitude and the highest rate (red histograms) was observed for those probes with low NND and high LCI, highlighting the multivariable nature of the rate constants.

Based on the histogram, we proposed a model to predict the single-molecule rate constant based on both NND and LCI. The Cox proportional hazard method (Cox PHM) is a multivariable method that uses a parametric linear combination of all risk factors to predict the survival rate in biology.[35] We applied the same concept to model the single-molecule rate constant using the following expression,

$$k_i = k_0 \exp\left(\alpha_{LCI} LCI_i + \beta_{NND}/NND_i\right) \quad (1)$$

where k_0 is the baseline rate constant, α_{LCI} and β_{NND} are regression parameters related to LCI and NND, respectively (Figure 4b). It should be noted that k_i converges into a constant baseline rate constant k_0 in isolation, where LCI = 0 and NND goes to infinity. To justify the use of the two-parameter (α_{LCI} and β_{NND}) Cox PHM model, we applied the Bayes-Schwartz Information Criterion (BIC)[36] in which the addition of a new parameter will decrease the negative log-likelihood by log(N)/2, where N is the total number of probes, i.e. the negative log-likelihood must be at least 3.8 (2044
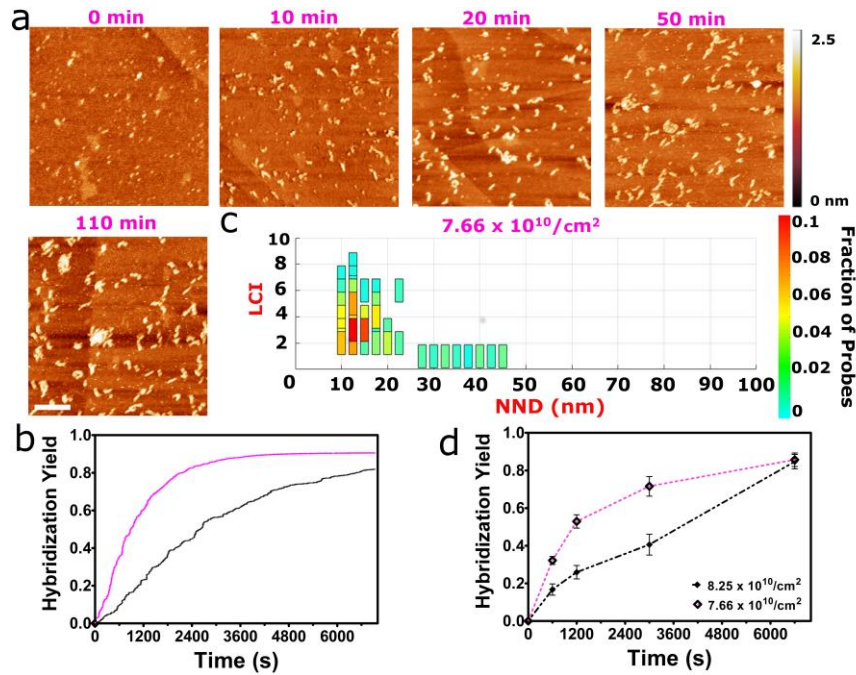

Figure 4. Modeling and predicting the overall hybridization kinetics based on local spatial pattern. (a) Rate constants (represented by color histograms) distribution of the probes as a function of both NND and LCI. (b) Cox proportional hazard fitting (pink surface) of the rate constants (green dots). (c) Numerical simulation of the overall kinetics using the single-molecule rate constants predicted by the Cox proportional hazard model at 1.83×10^{10} (cyan, S1), 4.44×10^{10} (blue, S2), 8.25×10^{10} (black, S3) and 2.03×10^{11} (green, S4) probes/cm².

probes in total) more than that of the null hypothesis ($\alpha_{LCI} = 0$ and $\beta_{NND} = 0$). We performed a maximum likelihood estimation (MLE) across all the probes using equation (1) and we find negative log-likelihood of 20.69 and 287.52 exceed those of the null hypothesis for α_{LCI} and β_{NND} respectively, justifying their appearance in single-molecule rate constant equation. Using the database of extracted single-molecule rate constants in Figure 4a, our model makes the prediction for k_i of an unknown hybridization reaction i. We found $k_0 = 650.7$ M^{-1}s^{-1}, $\alpha_{LCI} = 0.1083$ probe^{-1} and $\beta_{NND} = 22.01$ nm^{-1}. The obtained k_0 is similar to what has been observed for hairpin probes in solution.[37] These hairpin probes have lower rate constants than linear probes because unlike linear probes, the hybridization of hairpin probes requires the melting of the stem. The parameter β_{NND} corresponds to the length scale where the crowding interaction can influence hybridization. As the surface immobilized hairpin molecules can rotate around their anchor points, the contour length defines their "spheres of influence". The sphere of influence may grow after the probe molecule captures a target. Hence the presence of a hairpin molecule may alter the hybridization kinetics of another hairpin that is 20 nm away.

To connect these single-molecule behaviors in heterogeneous local environments to the overall hybridization kinetics, we incorporated the single-molecule rate constants predicted by our model into the numerical simulation that uses average rate constant to regenerate the overall kinetic trace (see SI for details), whose discrete nature adapts itself to handle discrete hybridization events. As depicted in Figure 4c, the simulated kinetics traces, resulting from an average over 100 simulations (Figure S4), well reproduced the experimental data in Figure 3a. This includes both the inhibition from 1.83×10^{10} to 8.25×10^{10} probes/cm^2 and acceleration at 2.03×10^{11} probes/cm^2. The discrepancy at 2.03×10^{11} probes/cm^2 may be attributed to the crowding effect that is introduced by the capture of

target molecules, which is difficult to accurately account for in the current model (a side-by-side comparison of AFM-derived kinetics to simulations is shown in Figure S5). The transition from a 23-base probe to an 82-base target-probe duplex notably increases the footprint. Hence, the probe molecules that were originally outside of the sphere of influence of a probe molecule with a contour length of 4-5 nm may encounter significantly more crowding interactions (electrostatic repulsion) once the probe captures a target with a contour length of 26 nm. Consequently, when more targets are hybridized, some of the neighboring probes may be destabilized, thereby reducing the activation barrier of stem melting and formation of target-probe duplex and accelerating the kinetics (Figure S7). This effect is most pronounced at the surface of 2.03×10^{11} probes/cm^2, which has a relatively high most probable NND (Figure 3a vs Figure 4c). A potential concern is that the unfolding of hairpins before target binding may adversely affect selectivity. The probe densities we studied (10^{10}-10^{11}/cm^2) are too low to cause a significant fraction of hairpins to unfold.[38] Previously we proposed that the acceleration of kinetics does not require complete unfolding of the hairpins. Instead, the acceleration of kinetics may be caused by the reduction in the activation barrier of stem melting due to the crowding interaction.[25] The selectivity of these hairpin probes can thus be retained during hybridization. Indeed, existing studies of E-DNA sensors did not observe mismatch selectivity to be significantly influenced by probe density in the range of 10^{10}-10^{12}/cm^2.[12, 39] That said, existing ensemble averaging methods cannot exclude the possibility that a small fraction of hairpin probes may experience stronger local interactions and lose some selectivity. Future spatial statistics studies will be needed to address this question. Currently, the limited spatial resolution makes it difficult to reliably incorporate the effect of target-induced crowding into our model. Because the target-probe duplex is significantly longer (26 nm), there is significant overlap between the features in the AFM image as the

Figure 5. Predicting the overall hybridization kinetics of surfaces with similar probe densities but different probe spatial patterns. (a-b) Representative AFM images and the corresponding numerical simulations of the kinetics of the sensor surface S5, in the presence of 100 nM target DNA at 7.66×10^{10} probes/cm^2 (purple solid line), which is similar to the surface density of S3, 8.25×10^{10} probes/cm^2 (black solid line). The scale bar is 100 nm. (c) Spatial organizations of the probes as a function of both NND and LCI. The color bar represents the range of fraction of probes. (d) Experimentally derived kinetics at 7.66×10^{10} (purple dash line) and 8.25×10^{10} (black dash line) probes/cm^2.

target molecules crowd the surface. As the spatial resolution of the AFM is about 3-5 nm, it becomes difficult to identify the tether points on this crowded surface and accurately measure NND and LCI. Therefore, both target-induced crowding effect and inaccurate identification of tether points can potentially be responsible for the discrepancy between experiment and simulation. The development of noncontact AFM that can potentially achieve sub-nanometer resolution will help us to understand hybridization on more crowded biosensor surfaces.[40-43]

Our initial success in reproducing the overall hybridization kinetics at different probe densities lends support to our hypothesis that the local spatial arrangement of the probes is a major determinant of the overall kinetics of the biosensor. However, the validity of the model needs to be independently tested on a new E-DNA sensor surface that has not been used to establish the model of single molecule rate constants. A surface (S5) with a probe density of 7.66×10^{10} probes/cm^2 (Figure 5a), which is close to its counterpart of 8.25×10^{10} probes/cm^2 in Figure 2c, was prepared by changing both the salt (NaAc) and probe concentrations during the insertion step (see experimental method section for details). Unlike its counterpart, which possesses a relatively uniform distribution of probes (Figure 2c), the surface featured highly clustered probes. This is supported by the spatial statistics illustrating a major population of probes with a low NND of 15 nm and a high LCI of 4 (Figure 5c), which deviates from its counterpart with a NND of 30 nm and a LCI of 1 or 2 in Figure 3b. Numerical simulation based on the spatial patterns and our phenomenological kinetic model showed that despite the similar probe surface density, the kinetic trace of S5 (purple solid curve in Figure 5b) would deviate significantly from the kinetic trace of S3 (Figure 4c or 5b). Due to the increased local crowding, the hybridization of S5 would be substantially faster than that of S3. Interestingly, the simulated traces in S5 (Figure 5b) was able to predict the major features of the experimental traces (Figure 5d), which is consistent with the nonmonotonic trend that the hybridization kinetics accelerates at high probe density in Figure 3a. The divergent kinetic traces of E-DNA sensor surfaces with similar average surface densities, but different spatial patterns constitute the clearest evidence that the average probe densities that are widely used[9-16, 34] do not serve as a reliable descriptor of the crowding interactions or predictor for the device performance. Together, these results revealed that the observed counter-intuitive overall kinetics of surfaces with similar or different probe densities are indeed a consequence of complex interactions comprising "two-body interactions" between nearest-neighboring probes, which depends on the inter-probe distance, and "many-body" interactions among the surrounding probes, which depends on the number of probes in a given area. Notably, while uniform probe densities are commonly considered to be more desirable because they are assumed to lead to more facile target capture for DNA sensors,[17, 44] the results herein paint a more complex picture. The more facile hybridization of S5 shows that some degree of probe clustering can accelerate surface hybridization of hairpin probes. Specifically, we can tailor the spatial pattern to have hairpin probes with inter-probe separations that favor the destabilization of neighboring probes surrounding captured targets and thus maximize target binding efficiency. The signal of an affinity biosensor is typically proportional to the number of target molecules captured.[23] Often it is too time consuming to allow the probe surface to reach equilibrium with the target molecules, i.e., the target capture is kinetically controlled. Hence the number of captured target molecules and by extension the sensitivity are determined by the rate of target recognition. Hence more facile target recognition is desirable as it improves the sensitivity or shortens detection time for a given sample. It should be noted that the spatial resolution of AFM does not allow us to measure NND values that are less than 5 nm, which become more prevalent at higher average probe densities, such as 10^{12}/cm^2. Therefore, our phenomenological model, in the present form, may fail at high probe density regimes because it does not account for the potential slow-down of hybridization at small NNDs due to steric hindrance. Improved imaging resolution will help to resolve probe molecules at more densely packed surfaces and enable the extension of the model to higher probe densities ($\sim 10^{12}$/cm^2 or higher).

CONCLUSION

In this study, high-resolution AFM imaging and a model of single-molecule rate constants were combined with numerical simulation, resulting in a framework that is capable of describing the overall hybridization kinetics on various E-DNA sensor surfaces. The first successful prediction of the kinetics of surface hybridization using the nanoscale structural information of the surface provide conclusive evidence that the spatial organization of the probe molecules is a major determinant of the performance of the devices. The framework established here provides a crucial starting point for more complex models. E.g., future studies that vary the lengths of the probes and targets may allow us to test more complex equations encompassing additional factors such as the crowding effect of the target molecules and potential coupling between LCI and NND. Moreover, the experimentally determined model of the single molecule rate constants in different local environments will serve as a benchmark to evaluate biophysical models[1, 28] that can help understand how crowding interactions influence interfacial molecular recognition and allow us to predict the behaviors of other types of DNA probes, such as linear probes, in crowded nanoscale environments. The molecular level understanding of the structure-function relationship of interfacial molecular recognition will help to unravel the origin of the significant device-to-device variabilities observed in many of the biosensors that use DNA probes as the recognition element.[20-24] Moreover, the fundamental understanding will enable new opportunities in improving the sensitivity and reproducibility of DNA biosensors and microarrays through rationally engineering of the spatial patterns of probe molecules using surface patterning techniques.[24, 44-45] The improvement in the performance of these biosensors can ultimately benefit the ultra-sensitive detection of biomarkers of infectious diseases and cancer. [5-8]

EXPERIMENTAL METHOD

Materials. Tris-(2-carboxyethyl) phosphine hydrochloride (TCEP) and 11-mercaptoundecanoic acid (MUDA) were purchased from Sigma-Aldrich Inc. (St. Louis, MO). 99.99% gold wire with 1mm diameter was purchased from Scientific Instrument Service (Ringoes, NJ). The oligonucleotide probe (HP) and target (T) with sequences summarized in Table S1 were synthesized by Biosearch Technologies, Inc. (Petaluma, CA) and Integrated DNA Technologies (Coralville, IA) respectively. Unless otherwise specified, all chemicals were purchased from Fisher Scientific Co. (Pittsburgh, PA).

E-DNA sensor fabrication and hybridization. To form the MUDA self-assembled monolayer, a gold bead containing single-crystal Au(111) facets prepared by melting the gold wire based on Clavier's method[46] was cleaned in hot nitric acid and flame-

annealed with hydrogen. The gold bead was then incubated overnight in a 1mM MUDA ethanolic solution that contains 10% (v/v) of acetic acid. After incubation, the gold bead was rinsed with 9:1 (v/v) ethanol:acetic acid, and then deionized water. The disulfide oligonucleotide probe (HP) was mixed with a TCEP reduction buffer for 20 min at room temperature in the dark. After reduction, the reaction mixture was purified using a QIAGEN nucleotide removal kit (Germantown, MD) and immediately used in all experiments. The MUDA functionalized gold bead was immersed in an insertion buffer for 30 min with the following composition: purified oligonucleotide probe, 2 mM TCEP and 50 mM NaAc (all E-DNA sensor surfaces except for S5 in Figure 5, which was prepared using 500 mM NaAc). The detailed insertion conditions used in this work were summarized in Table S2. All hybridization experiments were performed at a fixed target (T) concentration of 100 nM in the phosphate buffer (10 mM Phosphate, 1M NaAc, pH7) for a predetermined time. The gold bead was then thoroughly rinsed with an STAE buffer (1 x TAE, 200 mM NaAc) to remove the unbound oligonucleotide targets. To track the hybridization kinetics, the gold bead was completely submerged in an alkaline buffer containing 10 mM NaOH and 330 μM EDTA (pH10) for 5 min to denature the target-probe duplexes after each target incubation.

AFM measurement and image analysis. All AFM images were acquired with Ntegra Vita AFM (NT-MDT Co., Moscow, Russia) or Keysight 5500 AFM (Keysight Technologies, Santa Rosa, CA) under intermittent contact mode (tapping mode) with E-DNA sensor surface exposed to an imaging buffer of 5 mM $NiAc_2$ and 0.1 x TAE. SNL-10 AFM tips (Bruker, Bellerica, MA) with a spring constant of approximately 0.3 N/m were used in all experiments. STAE buffer was used to remove the remaining Ni^{2+} from the surface prior to each target incubation. All AFM images were first-order flattened using WSxM 5.0 software from Nanotec Electronica.[47] An average probe density was determined by manually masking the features of probes and automatically counting the total number of masks using Gwyddion (http://gwyddion.net/) in each AFM image. The XY-coordinates of the probes were extracted from the corresponding masks and used for NND and LCI analyses. The hybridization yield was determined by counting the number of target-probe duplexes and dividing it by the total number of probes.

ASSCOIATED CONTENT

Supporting Information

This material is available free of charge at

> For a detailed description of the materials and methods used in this work can be found in *SI Appendix*, which includes a descriptive list of all DNA oligonucleotides used, probe insertion conditions, DLS measurement, schematic of the crowding effect, DPV measurements, and details on Cox PHM and numerical simulation used to build the model for kinetics prediction (PDF).

AUTHOR INFORMATION

Corresponding Authors

Tao Ye – *Chemistry and Chemical Biology, School of Natural Sciences, University of California, Merced, Merced, California, 95343, United States*;
orcid.org/0000-0001-8615-3275; Email: tao.ye@ucmerced.edu

Authors

Qufei Gu - *School of Engineering, University of California, Merced, Merced, California, 95343, United States;*

Huan H. Cao - *Chemistry and Chemical Biology, School of Natural Sciences, University of California, Merced, Merced, California, 95343, United States;*

Yehan Zhang - *Chemistry and Chemical Biology, School of Natural Sciences, University of California, Merced, Merced, California, 95343, United States;*

Haiyang Wang - *School of Engineering, University of California, Merced, Merced, California, 95343, United States;*

Zachary J. Petrek - *Chemistry and Chemical Biology, School of Natural Sciences, University of California, Merced, Merced, California, 95343, United States;*

Fukun Shi - *Leibniz Institute for Plasma Science and Technology (INP), Greifswald, 17489, Germany;*

Eric A. Josephs - *Department of Nanoscience, University of North Carolina at Greensboro, Greensboro, North Carolina, 27401, United States;*

Notes

The authors declare no competing financial interests.

REFERENCES

1. Rao, A. N.; Grainger, D. W., Biophysical Properties of Nucleic Acids at Surfaces Relevant to Microarray Performance. *Biomater. Sci.* **2014,** *2* (4), 436-471.

2. Arroyo-Curras, N.; Somerson, J.; Vieira, P. A.; Ploense, K. L.; Kippin, T. E.; Plaxco, K. W., Real-Time Measurement of Small Molecules Directly in Awake, Ambulatory Animals. *Proc. Natl. Acad. Sci. USA* **2017,** *114* (4), 645-650.

3. Kelley, S. O., Advancing Ultrasensitive Molecular and Cellular Analysis Methods to Speed and Simplify the Diagnosis of Disease. *Acc. Chem. Res.* **2017,** *50* (3), 503-507.

4. Xi, Q.; Zhou, D. M.; Kan, Y. Y.; Ge, J.; Wu, Z. K.; Yu, R. Q.; Jiang, J. H., Highly Sensitive and Selective Strategy for Microrna Detection Based on Ws2 Nanosheet Mediated Fluorescence Quenching and Duplex-Specific Nuclease Signal Amplification. *Anal. Chem.* **2014,** *86* (3), 1361-1365.

5. Thomas, J. M.; Chakraborty, B.; Sen, D.; Yu, H. Z., Analyte-Driven Switching of DNA Charge Transport: De Novo Creation of Electronic Sensors for an Early Lung Cancer Biomarker. *J. Am. Chem. Soc.* **2012,** *134* (33), 13823-13833.

6. Feng, W.; Newbigging, A. M.; Le, C.; Pang, B.; Peng, H.; Cao, Y.; Wu, J.; Abbas, G.; Song, J.; Wang, D. B.; Cui, M.; Tao, J.; Tyrrell, D. L.; Zhang, X. E.; Zhang, H.; Le, X. C., Molecular Diagnosis of Covid-19: Challenges and Research Needs. *Anal. Chem.* **2020,** *92* (15), 10196-10209.

7. Wu, S. Y.; Yau, H. S.; Yu, M. Y.; Tsang, H. F.; Chan, L. W. C.; Cho, W. C. S.; Yu, C. S.; Yim, A.; Li, M.; Wong, Y. K. E.; Pei, X. M.; Wong, C. S. C., The Diagnostic Methods in the Covid-19 Pandemic, Today and in the Future. *Expert Rev. Mol. Diagn.* **2020**, DOI: 10.1080/14737159.2020.1816171.

8. da Silva, S. J. R.; da Silva, C. T. A.; Guarines, K. M.; Mendes, R. P. G.; Pardee, K.; Kohl, A.; Pena, L., Clinical and Laboratory Diagnosis of Sars-Cov-2, the Virus Causing Covid-19. *ACS Infect. Dis.* **2020**, DOI: 10.1021/acsinfecdis.0c00274.

9. Cederquist, K. B.; Golightly, R. S.; Keating, C. D., Molecular Beacon-Metal Nanowire Interface: Effect of Probe Sequence and

Surface Coverage on Sensor Performance. *Langmuir* **2008,** *24* (16), 9162-9171.

10. Cederquist, K. B.; Keating, C. D., Hybridization Efficiency of Molecular Beacons Bound to Gold Nanowires: Effect of Surface Coverage and Target Length. *Langmuir* **2010,** *26* (23), 18273-18280.

11. Peterson, A. W.; Heaton, R. J.; Georgiadis, R. M., The Effect of Surface Probe Density on DNA Hybridization. *Nucleic Acids Res.* **2001,** *29* (24), 5163-5168.

12. Ricci, F.; Lai, R. Y.; Heeger, A. J.; Plaxco, K. W.; Sumner, J. J., Effect of Molecular Crowding on the Response of an Electrochemical DNA Sensor. *Langmuir* **2007,** *23* (12), 6827-6834.

13. Herne, T. M.; Tarlov, M. J., Characterization of DNA Probes Immobilized on Gold Surfaces. *J. Am. Chem. Soc.* **1997,** *119* (38), 8916-8920.

14. Steel, A. B.; Herne, T. M.; Tarlov, M. J., Electrochemical Quantitation of DNA Immobilized on Gold. *Anal. Chem.* **1998,** *70* (22), 4670-4677.

15. Xu, F.; Pellino, A. M.; Knoll, W., Electrostatic Repulsion and Steric Hindrance Effects of Surface Probe Density on Deoxyribonucleic Acid (DNA)/Peptide Nucleic Acid (Pna) Hybridization. *Thin Solid Films* **2008,** *516* (23), 8634-8639.

16. Johnson-Buck, A.; Nangreave, J.; Jiang, S.; Yan, H.; Walter, N. G., Multifactorial Modulation of Binding and Dissociation Kinetics on Two-Dimensional DNA Nanostructures. *Nano Lett.* **2013,** *13* (6), 2754-2759.

17. Murphy, J. N.; Cheng, A. K. H.; Yu, H. Z.; Bizzotto, D., On the Nature of DNA Self-Assembled Monolayers on Au: Measuring Surface Heterogeneity with Electrochemical in Situ Fluorescence Microscopy. *J. Am. Chem. Soc.* **2009,** *131* (11), 4042-4050.

18. Josephs, E. A.; Ye, T., Nanoscale Spatial Distribution of Thiolated DNA on Model Nucleic Acid Sensor Surfaces. *ACS Nano* **2013,** *7* (4), 3653-3660.

19. Rao, A. N.; Rodesch, C. K.; Grainger, D. W., Real-Time Fluorescent Image Analysis of DNA Spot Hybridization Kinetics to Assess Microarray Spot Heterogeneity. *Anal. Chem.* **2012,** *84* (21), 9379-9387.

20. Bizzotto, D.; Burgess, I. J.; Doneux, T.; Sagara, T.; Yu, H. Z., Beyond Simple Cartoons: Challenges in Characterizing Electrochemical Biosensor Interfaces. *ACS Sensors* **2018,** *3* (1), 5-12.

21. Li, H.; Dauphin-Ducharme, P.; Ortega, G.; Plaxco, K. W., Calibration-Free Electrochemical Biosensors Supporting Accurate Molecular Measurements Directly in Undiluted Whole Blood. *J. Am. Chem. Soc.* **2017,** *139* (32), 11207-11213.

22. Yang, L.; Zhang, C. H.; Jiang, H.; Li, G. J.; Wang, J. H.; Wang, E. K., Insertion Approach: Bolstering the Reproducibility of Electrochemical Signal Amplification Via DNA Superstructures. *Anal. Chem.* **2014,** *86* (10), 4657-4662.

23. Du, H.; Disney, M. D.; Miller, B. L.; Krauss, T. D., Hybridization-Based Unquenching of DNA Hairpins on Au Surfaces: Prototypical "Molecular Beacon" Biosensors. *J. Am. Chem. Soc.* **2003,** *125* (14), 4012-4013.

24. Cao, H. H.; Nakatsuka, N.; Serino, A. C.; Liao, W. S.; Cheunkar, S.; Yang, H. Y.; Weiss, P. S.; Andrews, A. M., Controlled DNA Patterning by Chemical Lift-Off Lithography: Matrix Matters. *ACS Nano* **2015,** *9* (11), 11439-11454.

25. Gu, Q. F.; Nanney, W.; Cao, H. H.; Wang, H. Y.; Ye, T., Single Molecule Profiling of Molecular Recognition at a Model Electrochemical Biosensor. *J. Am. Chem. Soc.* **2018,** *140* (43), 14134-14143.

26. Fan, C.; Plaxco, K. W.; Heeger, A. J., Electrochemical Interrogation of Conformational Changes as a Reagentless Method for the Sequence-Specific Detection of DNA. *Proc. Natl. Acad. Sci. USA* **2003,** *100* (16), 9134-9137.

27. Morrin, G. M.; Schwartz, D. K., Three Regimes of Polymer Surface Dynamics under Crowded Conditions *Macromolecules* **2018,** *51* (3), 1207-1214.

28. Gong, P.; Levicky, R., DNA Surface Hybridization Regimes. *Proc. Natl. Acad. Sci. USA* **2008,** *105* (14), 5301-5306.

29. Vallee-Belisle, A.; Plaxco, K. W., Structure-Switching Biosensors: Inspired by Nature. *Curr. Opin. Struct. Biol.* **2010,** *20* (4), 518-526.

30. Abel, G. R., Jr.; Josephs, E. A.; Luong, N.; Ye, T., A Switchable Surface Enables Visualization of Single DNA Hybridization Events with Atomic Force Microscopy. *J. Am. Chem. Soc.* **2013,** *135* (17), 6399-6402.

31. Zuttion, F.; Redondo-Morata, L.; Marchesi, A.; Casuso, I., High-Resolution and High-Speed Atomic Force Microscope Imaging. *Methods Mol. Biol.* **2018,** *1814*, 181-200.

32. Yin, Y. D.; Zhao, X. S., Kinetics and Dynamics of DNA Hybridization. *Acc. Chem. Res.* **2011,** *44* (11), 1172-1181.

33. Gao, Y.; Wolf, L. K.; Georgiadis, R. M., Secondary Structure Effects on DNA Hybridization Kinetics: A Solution Versus Surface Comparison. *Nucleic Acids Res.* **2006,** *34* (11), 3370-3377.

34. Peterson, A. W.; Heaton, R. J.; Georgiadis, R., Kinetic Control of Hybridization in Surface Immobilized DNA Monolayer Films. *J. Am. Chem. Soc.* **2000,** *122* (32), 7837-7838.

35. Cox, D. R., Regression Models and Life-Tables. *J. R. Stat. Soc. B* **1972,** *34* (2), 187-220.

36. Schwarz, G., Estimating Dimension of a Model. *Ann. Stat.* **1978,** *6* (2), 461-464.

37. Tsourkas, A.; Behlke, M. A.; Rose, S. D.; Bao, G., Hybridization Kinetics and Thermodynamics of Molecular Beacons. *Nucleic Acids Res.* **2003,** *31* (4), 1319-1330.

38. Watkins, H. M.; Simon, A. J.; Ricci, F.; Plaxco, K. W., Effects of Crowding on the Stability of a Surface-Tethered Biopolymer: An Experimental Study of Folding in a Highly Crowded Regime. *J. Am. Chem. Soc.* **2014,** *136* (25), 8923-8927.

39. Ricci, F.; Zari, N.; Caprio, F.; Recine, S.; Amine, A.; Moscone, D.; Palleschi, G.; Plaxco, K. W., Surface Chemistry Effects on the Performance of an Electrochemical DNA Sensor. *Bioelectrochemistry* **2009,** *76* (1-2), 208-213.

40. Gross, L.; Mohn, F.; Moll, N.; Meyer, G.; Ebel, R.; Abdel-Mageed, W. M.; Jaspars, M., Organic Structure Determination Using Atomic-Resolution Scanning Probe Microscopy. *Nat. Chem.* **2010,** *2* (10), 821-825.

41. Gross, L.; Mohn, F.; Moll, N.; Liljeroth, P.; Meyer, G., The Chemical Structure of a Molecule Resolved by Atomic Force Microscopy. *Science* **2009,** *325* (5944), 1110-1114.

42. Asakawa, H.; Inada, N.; Hirata, K.; Matsui, S.; Igarashi, T.; Oku, N.; Yoshikawa, N.; Fukuma, T., Self-Assembled Monolayers of Sulfonate-Terminated Alkanethiols Investigated by Frequency Modulation Atomic Force Microscopy in Liquid. *Nanotechnology* **2017,** *28* (45), 455603.

43. Cao, H. H.; Abel, G. R., Jr.; Gu, Q.; Gueorguieva, G. V.; Zhang, Y.; Nanney, W. A.; Provencio, E. T.; Ye, T., Seeding the Self-Assembly of DNA Origamis at Surfaces. *ACS Nano* **2020,** *14* (5), 5203-5212.

44. Pei, H.; Lu, N.; Wen, Y. L.; Song, S. P.; Liu, Y.; Yan, H.; Fan, C. H., A DNA Nanostructure-Based Biomolecular Probe Carrier Platform for Electrochemical Biosensing. *Adv. Mater.* **2010,** *22* (42), 4754-4758.

45. Josephs, E. A.; Ye, T., Nanoscale Positioning of Individual DNA Molecules by an Atomic Force Microscope. *J. Am. Chem. Soc.* **2010,** *132* (30), 10236-10238.

46. Clavilier, J.; Faure, R.; Guinet, G.; Durand, R., Preparation of Mono-Crystalline Pt Microelectrodes and Electrochemical Study of the Plane Surfaces Cut in the Direction of the (111) and (110) Planes. *J. Electroanal. Chem.* **1980,** *107* (1), 205-209.

47.	Horcas, I.; Fernandez, R.; Gomez-Rodriguez, J. M.; Colchero, J.; Gomez-Herrero, J.; Baro, A. M., Wsxm: A Software for Scanning Probe Microscopy and a Tool for Nanotechnology. *Rev. Sci. Instrum.* **2007,** *78* (1), 013705.

For Table of Contents Only